DEVELOPMENT OF UNIFIED FRAMEWORK FOR MICROSTRUCTURE, RESIDUAL STRESS, AND CRACK PROPENSITY PREDICTION USING PHASE-FIELD SIMULATIONS

ALEXANDER STAROSELSKY[1], RANADIP ACHARYA[1] & BRICE CASSENTI[2]
[1] United Technologies Research Center.
[2] University of Connecticut.

ABSTRACT

The approach to obtain a specific user-defined/as-desired or conformal/epitaxial microstructure in additive manufacturing (AM) is a challenging and expensive iterative process. Modeling and validation of solidification microstructure and residual stresses can be leveraged to reduce iteration cost in obtaining as-desired microstructure, minimize residual stress and prevent hot cracking. In the present study, computational fluid dynamics analysis is used to predict melt pool characteristics, and phase-field modeling is employed to simulate solidification with corresponding microstructure evolution in the as-deposited state for laser powder bed fusion (LPBF) process. Different features of LPBF microstructure such as segregation of secondary elements, dendrite sizes, dendritic orientation and dendritic morphology are predicted. The methods are further extended to predict orientation change as a function of number of layers. A constitutive materials model coupled to solidification is used to predict the stress in as-built part as well as the effect of stress on microstructural features. The model encompasses the effect of thermo-mechanical and shrinkage stresses and considers creep flow due to the presence of liquid phases in the mushy region. A phase-field-based methodology is proposed that can solve for hot cracking starting from the intrinsic defects such as porosity in LPBF process. Depending on the residual stress, crack propagation can be predicted from the unified model. The model was incorporated in a finite element code and used to predict crack growth phenomena such as values of critical stress, crack path, etc. Phase-field models of crack growth reduce the computational complications associated with singularities and allow finite element predictions of crack propagation without remeshing. This work intends to develop a unified phase-field framework that can sequentially predict solidification microstructure, residual stresses and structural cracking.

Keywords: additive manufacturing, crack propagation, microstructure, phase field, residual stress, solidification.

1 INTRODUCTION

Additive manufacturing (AM) process allows fabrication of three-dimensional components layer by layer. In laser powder bed fusion (LPBF) processes, each layer is built by repeated melting and solidification of a powder bed using moving heat sources based on electron beam or laser beam. The solidification microstructure that develops during the process is influenced by the thermal history as well as the underlying structure in the previously solidified layer. The characteristics of the solidification microstructure including primary and secondary dendrite arms spacing, solute distribution within the dendrites and the dendrite orientations have a direct influence on the mechanical properties [1]. Therefore, it is essential to quantify the solidification microstructure in a given alloy, under a given set of processing parameters. A good review of the processing–structure relationships during AM of structural alloys is available in a recent publication [2].

LPBF is similar to the laser welding process, where the patch between surfaces of the original materials is filled layer by layer by solidified metal. Shrinkage during solidification and contraction due to rapid cooling of weld causes localized residual stresses. The variation

in temperature and shrinkage generates distribution of residual stresses in base metal and heat affected zone due to the constraints imposed on displacement by base metals. Experimental observations [3] show that high stresses together with various types of defects such as gas porosity, shrinkage pores, intergranular cracks and the presence of liquid films that occur at the solidified state [4] could cause the nucleation and propagation of the large hot crack. Hence, hot cracking is always related to thermomechanical conditions during AM that determines the local and global stresses and metallurgical aspects.

For choosing material processing parameters, a proper estimation of the effects of microstructures on mechanical behavior is required, because the microstructure of a material affects the macroscopic mechanical properties. Microstructure formed during solidification processes is caused by the cooling rate and can be predicted using various computational tools of which the phase-field model [5–6] is one of the most promising ones. In the binary phase-field method, the state of the entire microstructure is represented continuously by a single variable known as the order parameter, $0 \leq \phi \leq 1$. Bulk phases are represented by constant values of phase indicator, for example, in the liquid and the solid, while the interface corresponds to the domain where phase indicator changes. Thus, this mathematical formulation assumes a diffused interface or, in other words, it assumes that interfaces have finite thickness where physical quantities vary from their bulk values. The total free energy is then described in terms of the order parameter, ϕ, and its gradients. Phase-field (or diffuse) methods are based on minimization of the system free energy including gradients of the thermodynamic variables accounting for non-local effects. All state variables and parameters in this approach depend on the phase indicator, and subsequently, change with the evolution of the structure.

Stress distribution is strongly dependent on the morphology of the microstructure and, hence, varies due to mechanical anisotropy caused by dendritic growth from a crystallographic point of view. In this paper, we complement the free energy functional used for solidification microstructure prediction with elastic–viscoplastic terms caused by temperature variation and by the shrinkage caused by phase changes. After such a modification, the phase-field system of equations is able to predict residual stress distribution and the effect of residual stresses on microstructure evolution.

Predicting the failure of structural parts with complex material morphology and geometry is a challenging task. Usually, numerical approaches such as the finite element method (FEM) [7–8], boundary elements (BEMs) [9], or their hybrids [10–11] are used to predict crack path and critical values of applied loads. Fracture mechanics numerical simulations require re-meshing to handle crack propagation resulting in lengthy computational times. Yet, these methods do not accurately predict the instabilities at the crack tips, nor do they accurately predict the crack tip velocity. All this motivates researchers to consider alternative approaches for crack propagation that complement existing computational methods. Natural extensions of non-local methods include attempts to represent crack growth by phase-field equations, see for example [12–14].

Pristine material is represented by a constant value of phase indicator, taken to be equal to 1. The interior of a crack is represented by the value $\psi = 0$, while the interface corresponds to the domain where phase indicator changes (i.e. $0 \leq \psi \leq 1$). It can be seen as a gradual change of damage in the process zone decreasing away from the crack tips. However, the formulation of the energy density functional in the fracture mechanics literature is still to some extent empirical. An understanding of the model's physical basis and an accurate definition of the physical properties used in the energy density potential is crucial for correct problem formulation.

In the present paper, we develop a unified computational framework based on the phase-field approach to predict hot crack propagation during AM or laser welding. The phase-field formalism is first used to predict solidification microstructure and the corresponding residual stresses. The calculated stresses are applied to the micro defect/pore that can be anticipated in the solid structure based on the microstructure analysis. These stresses cause crack emanating from the pores, and crack growth is evaluated using the same mathematical/computational formalism. Hence, the whole problem from solidification dynamics to hot cracking is described in a unified manner.

The plan of the paper is as follows: In the next section, the phase-field model describing the solidification process and the resulting microstructure is described. The model is coupled with stress analysis and viscous flow for the liquid phase. In Section 3, the phase-field model for crack propagation is presented. The results of the computation of solidification and hot cracking are shown in Section 4, followed by the summary and concluding remarks.

2 MICROSTRUCTURE EVOLUTION IN LASER POWDER BED FUSION

The difference in thermal gradient and solidification speed due to different process parameter in laser powder bed fusion (LPBF) can cause changes in solidification microstructure. In order to understand the microstructural complexity, an experimental microstructure is presented first and then phase-field model is proposed for a simplified Ni–5Nb binary alloy mimicking IN718.

2.1 Experimental

The LPBF experiments were performed with an EOS M280 (EOS GmbH Electro Optical Systems; Munich Germany) LPBF unit that was fed with IN718 powder. The test results analysed in this paper are obtained from single track specimen deposited on top of an additively constructed base pad. After deposition, the build articles were sectioned, mounted, and polished for metallography. Figure 1(a) shows a representative single track deposit and 1(b) shows a section of a cube built with 67° scan rotation across layers.

Transverse cross sections of the single track specimens were imaged using a Helios Nanolab 600 dual beam microscope (FEI; Hillsboro, OR). The gallium ion beam was employed to local etch the surface of the coupon to discern dendrites better. The composition was probed using an X-MaxN 80 Energy Dispersive Spectroscopy (EDS) unit (Oxford Instruments; Concord, MA).

Figure 1c shows the segregation profile for Ni and Nb across primary arms for a representative sample. For line scans across primary arms, the Nb composition varies from ~4.0 wt.% at dendrite core to 8.0–9.0 wt.% at the interdendritic region.
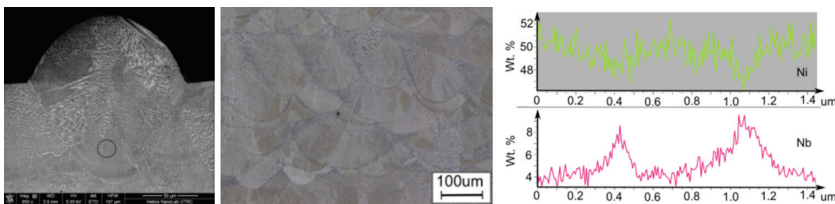
Figure 1: (a) Melt pool in LPBF process (left), (b) overlap of melt pool due to scan rotation across layers (middle) and (c) EDS map representing Ni and Nb segregation across primary dendrite arm (right).

2.2 Microstructure evolution model

Computation fluid dynamics models are used to compute the shape and conditions in the so-called mushy zone where solidification takes place. The details of the modeling scheme are described elsewhere [6]. Figure 2 shows computational fluid dynamics (CFD) simulation results for a representative melt pool evolution and mushy zone formation behind the melt pool.

Phase-field analysis was carried out on an undercooled mushy region since the high temperature inside the melt pool does not allow nucleation of the dendrites. The model adopted here is based on Kobayashi [15] and Boettinger *et al.* [16] formulations corrected for materials anisotropy based on Zaeem *et al.* [17] approach. In the phase-field model, the state at each point is described by a single valued scalar, $0 \leq \phi \leq 1$, where $\phi = 0$ represents a fully melted state and $\phi = 1$ represents a fully solidified one. We solved a coupled systems of equations in (ϕ, T, c) as explained in [6]:

$$\tau_c \frac{\partial \varphi}{\partial t} = \tilde{\varepsilon}^2 \nabla \cdot \left(\begin{pmatrix} \sigma^2 & -\sigma\sigma' \\ \sigma\sigma' & \sigma^2 \end{pmatrix} \nabla \varphi \right) + \varphi(1-\varphi)\left(\varphi - \frac{1}{2} + m \right) + \tau_c v_x \frac{\partial \varphi}{\partial x} \tag{1}$$

$$\frac{\partial T}{\partial t} - v_x \frac{\partial T}{\partial x} = a_T \nabla^2 T + \frac{L}{C_p}\frac{\partial \varphi}{\partial t} - \frac{Lv_x}{C_p}\frac{\partial \varphi}{\partial x} \tag{2}$$

$$\frac{\partial c}{\partial t} = \bar{\nabla} \cdot \left[\varphi D_S \bar{\nabla} c_s + (1-\varphi)D_L \bar{\nabla} c_L \right] + v_x \frac{\partial C}{\partial x} \tag{3}$$

where v_x is the scan speed in the *x*-direction. Eqns (1)–(3) are normalized as follows:

$$T = \frac{T_{actual} - T_S}{T_L - T_S}, x = x_{actual} / l_0, t = t_{actual} / \tau.$$
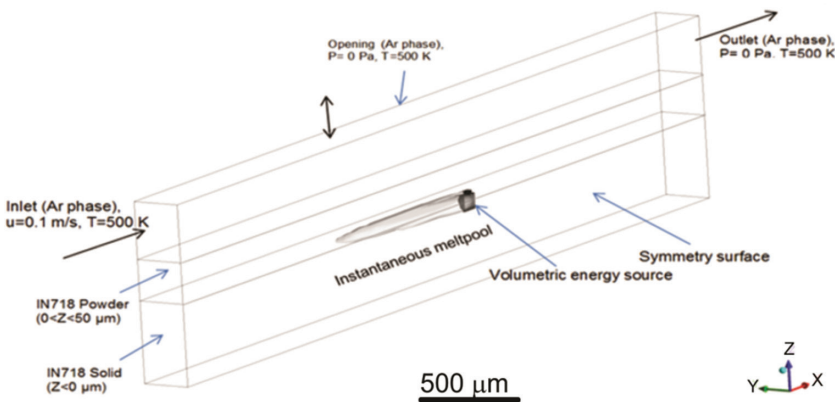
Figure 2: CFD simulation of melting in AM process. The meshed region indicates the remelted zone in the powder and substrate layer and the instantaneous melt pool is progressively dark colored.

Here, l_0 is characteristic length scale and t characteristic time scale equals to $l_0{}^2/\partial_t$. c_S and c_L represents concentration of Nb in solid and liquid respectively, α_T is thermal diffusivity, L is latent heat, C_p is specific heat, D_L and D_S represents solid and liquid diffusivity respectively. Also, $\sigma = f(j, \delta, \theta)$, where j represents order of symmetry, δ represents strength of anisotropy and θ represents angle of growth direction with horizontal. The normalized scan velocity is,

$$\tilde{v}_x = \frac{v\,\tau}{l_0}.$$

The numerical solution in 3D is very expensive and time-consuming; therefore, the problem was divided into two 2D problems in corresponding orthogonal cross sections. The first cross-section is in the transverse direction (y–z plane in Fig. 2). By solving this "transverse" plane problem, we assume that all cross-sections have the same solidification pattern. Such an assumption allows quasi-steady state formulation, which does not include the laser source velocity. The second cross-section is in the scan velocity direction or longitudinal plane (x–z plane in Fig. 2). This problem requires a direct account for the effect of moving heat source.

In order to calibrate the numeral coefficients in the phase-field model, a single dendrite simulation is first carried out in an undercooled melt. The transient evolution of the order parameter ϕ and concentration field of secondary element Nb is observed as shown in Fig. 3.

The transverse cross-section provides an evolution of microstructure in a stationary domain. Flux boundary condition corresponding to CFD solution has been applied on the top surface. Figure 4(a) shows the evolution of columnar dendritic structure in the presence of higher undercooling (~200 K). As the undercooling is reduced the morphology transitions from columnar dendrites to columnar, that does not show any secondary arms. However, Nb segregations are observed between the primary trunks. In addition, based on the temperature gradient at the top and bottom surface, a different spacing of the primary trunks is obtained. Lower temperature gradient at the top surface can create coarser dendrites when compared to the dendrites growing from the bottom of the mushy zone.

The analysed effect of scan velocity can be easily extended to include progressive change in dendritic orientation in multilayer build. Dendrites developed during the first solidification track (1st layer) start with zero misorientation from the vertical axis, possesses an average of 20° misorientation with vertical direction in the final microstructure. This was then used as initial misorientation for the 2nd layer, and the final misorientation angle is 25°. For 3rd and 4th layer values of 27° and 28° have been obtained. If the scan velocity direction is rotated, that will cause overlapping of the patchy texture as shown in Fig. 1b. Figure 5a compares the dendrite misorientation with the experimental dendrite orientation in Fig. 5b.
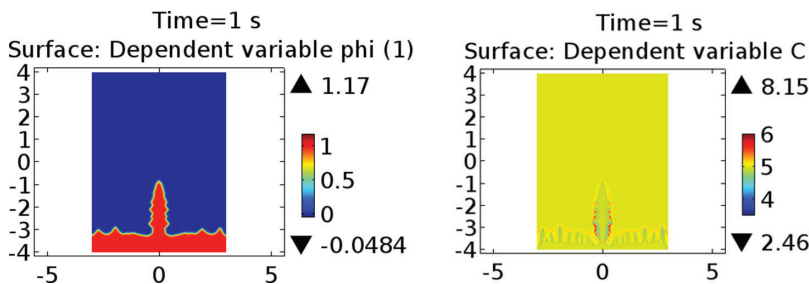
Figure 3: (a) Growth of singular dendrite (left) and (b) concentration of Nb around dendrite (right).
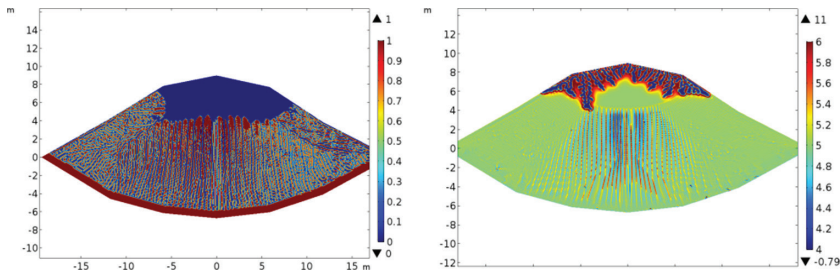
Figure 4: (a) Columnar dendritic growth (left) and (b) columnar growth (right).
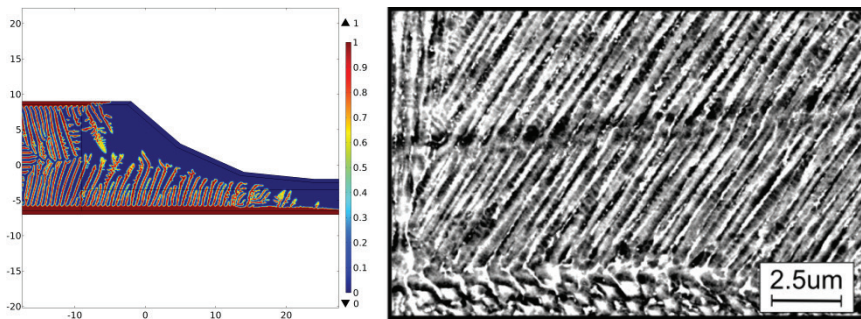
Figure 5: (a) Evolution of dendrite orientation as a function of initial orientation in layer 4 (left) and (b) experimental dendrite orientation in LPBF (right).

3 RESIDUAL STRESS PREDICTION IN AM

To introduce the residual stress development in the phase-field framework, strain energy is included in the total energy formulation which is minimized to derive the equation for the order parameter. The material properties are also formulated as a function of order parameter within the constitutive stress–strain relation. Section 3.1 briefly highlights the model development and Section 3.2 describes the prediction of residual stress during the LPBF process.

3.1 Model development

The total energy of the system with the inclusion of strain energy can be written as

$$E = \int_V \left[\frac{1}{2} k (\nabla \phi)^2 + V(\phi, T, C) + F(T, \sigma, \varepsilon, \phi) \right] dV \tag{4}$$

The strain energy F can further be computed as

$$F = F_{thermal} + F_{elastic} + F_{Shrinkage} \tag{5}$$

In the formulation, the modulus is included as a function of the order parameter, as an example, the shear modulus is written as

$$G = p \cdot G_s + (1 - p) \cdot G_l \tag{6}$$

where

$$p = \phi^3 \left(10 - 15\phi + 6\phi^2\right)$$

Subscripts s and l indicate solid and liquid phases, respectively, and in the present formulation, we assumed, $G_l = G_s/10$. For bulk modulus K, we assumed, $K_l = K_s$

The contribution of thermal, elastic and shrinkage components are computed separately according to

$$F_{thermal} = -K\alpha\left(T - T_l\right)\varepsilon_{kk}, \quad F_{shrinkage} = \beta\phi K \varepsilon_{kk}. \tag{7}$$

Here

$$\beta = -\frac{1}{3}\left(1 - \frac{\rho_l}{\rho_s}\right)$$

The compatibility equations are

$$\varepsilon_{ij} = \frac{1}{2}\left(u_{i,j} + u_{j,i}\right) \tag{8}$$

denoting the strain-displacement relation. The equilibrium is written as

$$\sigma_{ij,j} = 0 \tag{9}$$

Eqn (4) also creates an additional source term in the right-hand side of eqn (1) as,

$$\phi_{FS} = \frac{d^2}{\Gamma}\frac{\partial F}{\partial \phi} \tag{10}$$

where

$$d = 1.415 \cdot 10^{-8}, \Gamma = 3.65 \cdot 10^{-7}$$

The shrinkage strain can often exceed 3% to accommodate the large strain the liquid phase can flow. This necessitates the use of creep model to reduce the stress magnitude. Norton model is used in the COMSOL Multiphysics solver for this purpose [18] with the following parameters shown in Table 1.

Table 1: Creep model parameter in Norton model.

Parameter	Magnitude
Creep rate coefficient, A	3×10^{-6}
Reference creep stress, σ_{ref}	1 [MPa]
Stress exponent, n	3
Creep activation energy, Q	2.64×10^4[J/mol]*p+2.64×10^3[J/mol]*$(1-p)$

3.2 Stress prediction

The framework described in Section 3.1 is implemented along with the coupled framework for microstructure evolution in COMSOL for dendrites growing from two opposing surfaces. The results are presented in Fig. 6. With increasing time, the primary dendrite trunk starts to coarsen for $t = 1$ in Fig. 6b. The corresponding stress contours are shown in Fig. 6c and d. As seen, the higher stresses are observed near the interfaces. For the representative case, the stress is in the order of 300 MPa. Similar magnitudes of stresses are also reported elsewhere without using phase field [19].

Figure 7 shows results for multiple dendrites growth and the resultant stress field. It is seen that stresses are still high at the interface and the intersection of dendrites creates the stress hotspots even in the liquid metal as shown in Fig. 7d. This potentially can create hot cracks or porosity due to the tensile stresses applied to liquid material.

4 CRACK PROPAGATION MODEL

LPBF is susceptible to defects such as unmelt/lack of fusion and keyhole porosities if the energy density is either too small or too large respectively. That leads to pores inside the structural part that can act as a stress risers. These defects combined with the residual stress
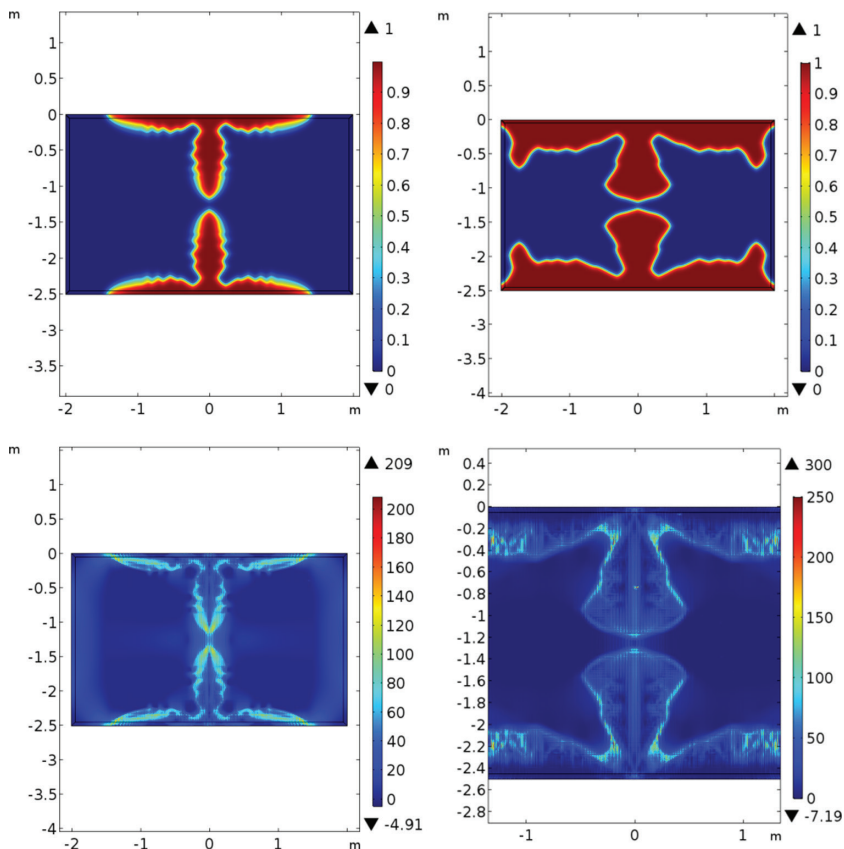
Figure 6: Transient growth of dendrite at normalized time (a) t=0.2 (top left), (b) t=1(top right), and first principal stress distribution in MPa at (a) t=0.2 (bottom left), (b) t=1 (bottom right).
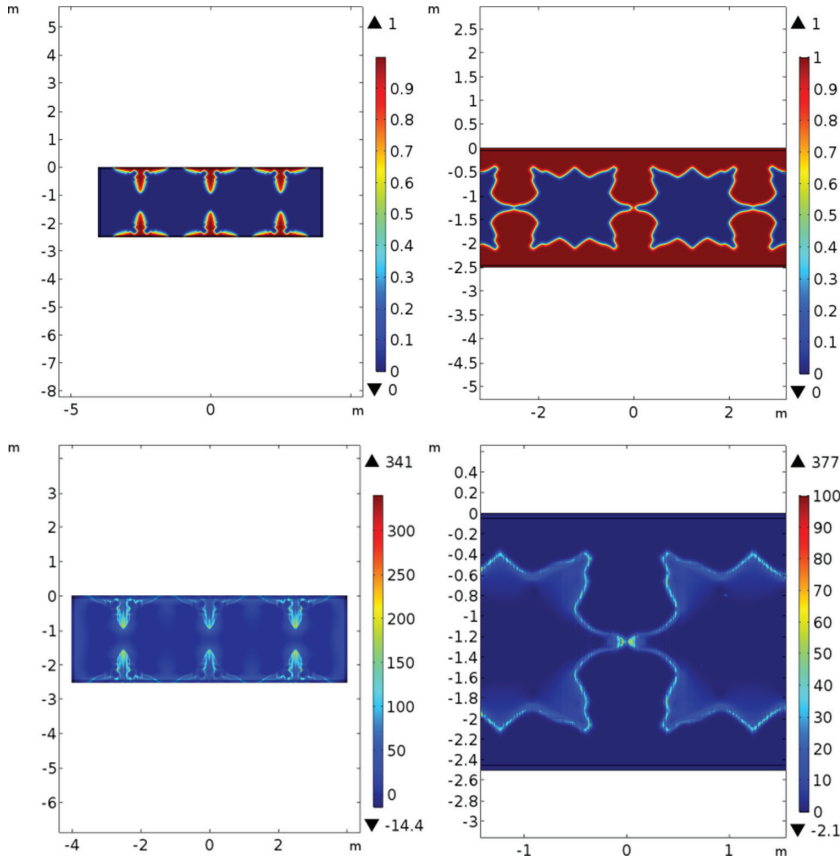
Figure 7: Transient growth of dendrite at normalized time (a) t=0.1 (top left) , (b) t=5 (top right) ,and first principal stress distribution in MPa at time (a) t=0.1 (bottom left), stresses in unsolidified region at (b) t=5 (bottom right).

often leads to hot cracking. Next section would focus on developing a phase-field-based crack propagation model to predict crack propagation path due to the tensile residual stresses.

4.1 Model development

A governing equation based on Lagrangian density is proposed, and the phase evolution is shown to be governed by a diffusion type equation with a source term as

$$E_0 \tau_1 \frac{\partial \psi}{\partial t} = D_1 \frac{\partial}{\partial x_i} \left(n_i n_j \frac{\partial \psi}{\partial x_j} \right) - V'_{DW}(\psi) - \frac{1}{2} \frac{\partial \sigma_{ij}}{\partial \psi} \varepsilon_{ij} \qquad (11)$$

where ψ is the order parameter ($\psi = 0$ represents crack and $\psi = 1$ represents pristine material), n_k is a unit normal vector in the direction of the minimum principal stress, $E_0 \tau_1$ is material constant and σ_{ij}, ε_{ij} represent the stress and strain field, respectively. The diffusion coefficient D_1 and double-well potential, V_{DW} can be defined using the following formulation [12, 14] as

$$D_1 = \gamma \varepsilon, V_{DW} = \frac{\gamma}{\varepsilon} V_{pot}(\psi) \tag{12}$$

where γ is the crack surface energy and ε represents the interface thickness. $V_{pot}(\phi)$ is expressed as

$$V_{pot} = V_0(1-\psi)^2 \left(1+2\psi+C\psi^2\right) \tag{13}$$

The moduli are written as a function of order parameter as

$$G(\psi) = G_0 \left(4\psi^3 - 3\psi^4\right), \quad K(\psi) = K_0 \left(4\psi^3 - 3\psi^4\right) \tag{14}$$

where G and K represent shear and bulk modulus, respectively, and the G_0 and K_0 represent moduli corresponding to the pristine condition. Further details of the model including parameters magnitude can be found in [12]. In the next section, a crack propagation analysis from a representative pore in the LPBF process is presented.

4.2 Results and discussion

The methodology described in Section 4.1 has been used to predict crack propagation and critical stress evaluation for different load configuration. One such example is presented in Fig. 8 for non-straight crack growth due to pure shear load and the predicted stress distribution. Of particular importance, is that the simulated crack shows the initial fracture angle to be within 69°–70°, which agrees well with results from fracture mechanics modeling and experiments [20–21]. Also, the bending of crack to 45° can be observed upon further growth, which is expected because crack finally aligns itself perpendicular to the maximum principal stress.

This methodology is used for a representative AM sample. The geometry of the crack configuration is shown in Fig. 9a, corresponding to interacting cracks emanating from pores of size 500 μm and with an initial crack size of 1.25 mm. LEFM results predict the critical stress of 249.53 MPa for the given configuration and crack size [22]. This represents the simulation shown in Fig. 8 due to the interaction of multiple dendrites and potential porosity or cracks rising from dendrites collision.

Figure 9c shows the variation of crack propagation velocity with loading. As seen, a jump in propagation velocity occurs at a critical load of 250 MPa. However, at higher load the crack starts to bifurcate, resulting in the reduction of crack propagation velocity.
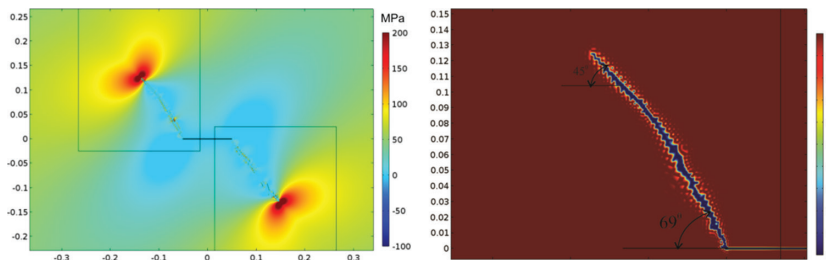
Figure 8: (a) First principal stress distribution (left) and (b) measured
angle under crack propagation due to pure shear load (right).
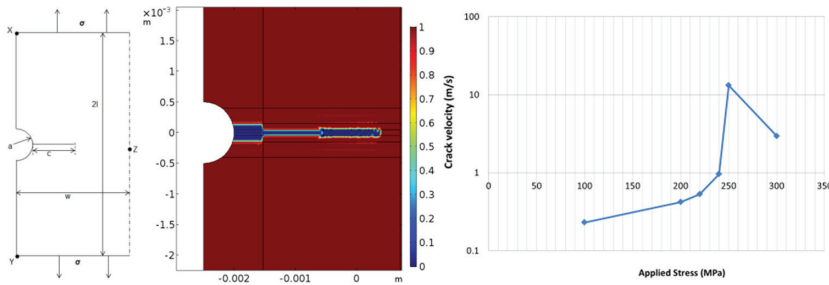
Figure 9: (a) Crack configuration and boundary condition (left), (b) crack propagation at $\sigma = 250$ MPa (middle) and (c) Variation of propagation velocity with load, σ (right).

5 CONCLUSIONS

In the present work, we established a methodology of utilizing a phase-field-based method to predict the microstructure, residual stress and crack propagation path starting from intrinsic defects in the AM process. The method shows success in the prediction of Nb concentration, dendrite misorientation in columnar dendritic structure. Simultaneous solution of stress afield enabled the computation of residual stresses during the LPBF process that can lead to potential hot cracking and porosity. The method shows a realistic prediction of stresses during deposition. A conceptual example of a crack emanating from AM intrinsic defect is later simulated. The result shows the residual tensile stress can cause hot cracking if the defects are of a certain size and the methodology can predict the critical stresses in that configuration. A unified framework thus can be proposed to predict hot cracking defects in LPBF process based on the phase field and will be pursued in the future.

REFERENCES

[1] Radhakrishnan, B., Gorti, S.B., Turner, J.A., Acharya, R., Sharon, J.A., Staroselsky, A. & El-Wardany, T., Phase Field Simulations of Microstructure Evolution in IN718 using a Surrogate Ni–Fe–Nb Alloy during Laser Powder Bed Fusion. *Metals*, **9(1)**, pp. 14–41, 2018. https://doi.org/10.3390/met9010014

[2] DebRoy, T., Wei, H.L., Zuback, J.S., Mukherjee, T., Beese, A.M., Wilson-Heid, A., Elmer, J.W., Milewski, J.O., De, A. & Zhang, W., Additive manufacturing of metallic components – Process, structure and properties. *Progress in Materials Science*, **92**, pp. 112–224, 2018. https://doi.org/10.1016/j.pmatsci.2017.10.001

[3] Chauvet, E., Kontis, P., Jagle, E. A., Gault, B.,Raabe, D., Tassin, C., Blandin, J., Dendievel, R., Vayre, B., Abed, S. & Martin, G., Hot cracking mechanism affecting a non-weldable Ni-basedsuperalloy produced by selective electron Beam Melting. *Acta Materialia*, **142**, pp. 82–94, 2018. https://doi.org/10.1016/j.actamat.2017.09.047

[4] Langrieger, H., Krafft, F., Mensinger, M. & Oefele, F., Thermomechanical analysis of the formation of hot cracks in remote laser welded aluminium fillet welds. *Journal of Laser Applications*, **28(2)**, pp. 022414-1–022414-7, 2016. https://doi.org/10.2351/1.4944093

[5] Uehara, T., Fukui, M. & Ohno, N., Phase field simulations of stress distributions in solidification structures. *Journal of Crystal Growth,* **310(7–9)**, pp. 1331–1336, 2008. https://doi.org/10.1016/j.jcrysgro.2007.12.035

[6]   Acharya, R., Sharon, J.A. & Staroselsky, A., Prediction of microstructure in laser powder bed fusion process. *Acta Materialia*, **124**, pp. 360–371, 2017. https://doi.org/10.1016/j.actamat.2016.11.018

[7]   Bathe, K.J., *Finite Element Procedures*, Prentice-Hall, Englewood Cliffs, NJ, 1996.

[8]   Du, Z.Z., Extended Finite Element Method (XFEM) in Abaqus. Dassault Syst Online: www.simulia.com/download/rum11/UK/Advanced-XFEM-Analysis.pdf (accessed 18 March, 2019).

[9]   Katsikadelis, J.T., *The Boundary Element Method for Engineers and Scientists: Theory and Applications*, Academic Press, London, UK, 2016.

[10] Annigeri, B.S. & Cleary, M.P., Surface integral finite element hybrid (SIFEH) method for fracture mechanics. *International Journal for Numerical Methods in Engineering,* **20(5)**, pp. 869–885, 1984. https://doi.org/10.1002/nme.1620200507

[11] Forth, S.C. & Staroselsky, A., A hybrid FEM/BEM approach for designing an aircraft engine structural health monitoring. *Computer Modeling in Engineering and Sciences*, **9(3)**, pp. 287–298, 2005.

[12] Staroselsky, A., Acharya, R. & Cassenti, B., Phase field modeling of fracture and crack growth. *Engineering Fracture Mechanics*, **205**, pp. 268–284, 2019. https://doi.org/10.1016/j.engfracmech.2018.11.007

[13] Hakim, V. & Karma, A., Laws of crack motion and phase-field models of fracture. *Journal of the Mechanics and Physics of Solids*, **57(2)**, pp. 342–368, 2009. https://doi.org/10.1016/j.jmps.2008.10.012

[14] Levitas V.I., Jafarzadeh, H., Farrahi, G.H. & Javanbakht, M., Thermodynamically consistent and scale-dependent phase field approach for crack propagation allowing for surface stresses. *International Journal of Plasticity*, **111**, pp. 1–35, 2018. https://doi.org/10.1016/j.ijplas.2018.07.005

[15] Kobayashi, R., Modeling and numerical simulations of dendritic crystal growth. *Physica D: Nonlinear Phenomena*, **63(3–4)**, pp. 410–423, 1993. https://doi.org/10.1016/0167-2789(93)90120-p

[16] Boettinger, W.J., Warren, J.A., Beckermann, C. & Karma, A., Phase-field simulation of solidification. *Annual Review of Materials Research,* **32(1)**, pp. 163–194, 2002. https://doi.org/10.1146/annurev.matsci.32.101901.155803

[17] Zaeem, M.A., Yin, H. & Felicelli, S., Modeling dendritic solidification of Al–3% Cu using cellular automaton and phase-field methods. *Applied Mathematical Modelling*, **37(5)**, pp. 3495–3503, 2013. https://doi.org/10.1016/j.apm.2012.08.005

[18] COMSOL M. 3.3: Manual, *Structural Mechanics Module*, pp. 323–346, 2006.

[19] Megahed, M., Mindt, H.W., N'Dri, N., Duan, H. & Desmaison, O., Metal additive-manufacturing process and residual stress modeling. *Integrating Materials and Manufacturing Innovation*, **5(4)**, pp. 1–33, 2016. https://doi.org/10.1186/s40192-016-0047-2

[20] Cherepanov G.P., *Mechanics of Brittle Fracture*, McGraw-Hill, New York, 1979.

[21] Staroselsky, A., Damage and cracking morphology. *Advances in Fatigue, Fracture and Damage Assessment of Materials*, pp. 15–53, 2005. https://doi.org/10.2495/1-85312-836-8/02

[22] Yamamoto, Y., Sumi, Y. & Ao, K., Stress intensity factors of cracks emanating from semi-elliptical side notches in plates. *International Journal of Fracture*, **10(4)**, pp. 593–595, 1974. https://doi.org/10.1007/bf00155263